**ORCA – Online Research @ Cardiff** 



This is an Open Access document downloaded from ORCA, Cardiff University's institutional repository:https://orca.cardiff.ac.uk/id/eprint/109936/

This is the author's version of a work that was submitted to / accepted for publication.

Citation for final published version:

Manga, Michael, Fauria, Kristen E., Lin, Christina, Mitchell, Samuel J., Jones, Meghan, Conway, Chris E., Degruyter, Wim, Hosseini, Behnaz, Carey, Rebecca, Cahalan, Ryan, Houghton, Bruce F., White, James D.L., Jutzeler, Martin, Soule, S. Adam and Tani, Kenichiro 2018. The pumice raft-forming 2012 Havre submarine eruption was effusive. Earth and Planetary Science Letters 489, pp. 49-58. 10.1016/j.epsl.2018.02.025

Publishers page: http://dx.doi.org/10.1016/j.epsl.2018.02.025

# Please note:

Changes made as a result of publishing processes such as copy-editing, formatting and page numbers may not be reflected in this version. For the definitive version of this publication, please refer to the published source. You are advised to consult the publisher's version if you wish to cite this paper.

This version is being made available in accordance with publisher policies. See http://orca.cf.ac.uk/policies.html for usage policies. Copyright and moral rights for publications made available in ORCA are retained by the copyright holders.



1	The pumice raft-forming 2012 Havre submarine eruption was effusive
2	
3	Michael Manga <sup>1*</sup> , Kristen E. Fauria <sup>1,3</sup> , Christina Lin <sup>1</sup> , Samuel J. Mitchell <sup>2</sup> , Meghan Jones <sup>3</sup> , Chris
4	Conway <sup>4</sup> , Wim Degruyter <sup>5</sup> , Behnaz Hosseini <sup>1</sup> , Rebecca Carey <sup>6</sup> , Ryan Cahalan <sup>7</sup> , Bruce F.
5	Houghton <sup>2</sup> , James D.L. White <sup>8</sup> , Martin Jutzeler <sup>6</sup> , S. Adam Soule <sup>3</sup> , Kenichiro Tani <sup>4</sup>
6	
7	1 Department of Earth and Planetary Science, University of California, Berkeley, CA 94720,
8	USA
9	2 Department of Geology and Geophysics, University of Hawai'i at Mānoa, 1680 East West
10	Road, Honolulu, HI 96822, USA
11	3 Woods Hole Oceanographic Institution, Woods Hole, MA 02543, USA
12	4 National Museum of Nature and Science, 4-1-1 Amakubo, Tsukuba, Ibaraki 305-0005, Japan
13	5 School of Earth and Ocean Sciences, Cardiff University, Main Building, Park Place, Cardiff,
14	CF10 3AT, Wales, UK
15	6 School of Physical Sciences and Centre of Excellence in Ore Deposits (CODES), University of
16	Tasmania, Hobart, TAS 7001, Australia
17	7 School of Earth and Atmospheric Sciences, Georgia Institute of Technology, 311 Ferst Drive,
18	Atlanta, GA 30332, USA
19	8 Department of Geology, University of Otago, PO Box 56, Dunedin 9054, New Zealand
20	
21	*Corresponding author, manga@seismo.berkeley.edu

January 17, 2018, revised February 13, 2018 

#### 25 Abstract

26

27 A long-standing conceptual model for deep submarine eruptions is that high hydrostatic pressure 28 hinders degassing and acceleration, and suppresses magma fragmentation. The 2012 submarine 29 rhyolite eruption of Havre volcano in the Kermadec arc provided constraints on critical 30 parameters to quantitatively test these concepts. This eruption produced  $a > 1 \text{ km}^3$  raft of floating pumice and a 0.1 km<sup>3</sup> field of giant (>1 m) pumice clasts distributed down-current from the vent. 31 32 We address the mechanism of creating these clasts using a model for magma ascent in a conduit. 33 We use water ingestion experiments to address why some clasts float and others sink. We show 34 that at the eruption depth of 900 m, the melt retained enough dissolved water, and hence had a 35 low enough viscosity, that strain-rates were too low to cause brittle fragmentation in the conduit, 36 despite mass discharge rates similar to Plinian eruptions on land. There was still, however, 37 enough exsolved vapor at the vent depth to make the magma buoyant relative to seawater. 38 Buoyant magma was thus extruded into the ocean where it rose, quenched, and fragmented to 39 produce clasts up to several meters in diameter. We show that these large clasts would have 40 floated to the sea surface within minutes, where air could enter pore space, and the fate of clasts 41 is then controlled by the ability to trap gas within their pore space. We show that clasts from the 42 raft retain enough gas to remain afloat whereas fragments from giant pumice collected from the 43 seafloor ingest more water and sink. The pumice raft and the giant pumice seafloor deposit were 44 thus produced during a clast-generating effusive submarine eruption, where fragmentation 45 occurred above the vent, and the subsequent fate of clasts was controlled by their ability to ingest 46 water.

_ /	~
71	- 1
-	1

48	Keywords: submarine eruption; pumice; fragmentation; raft; conduit flow; X-ray tomography
49	
50	Highlights:
51	Havre magma entered the ocean before fragmenting.
52	Clasts were produced by quenching buoyant magma in the ocean.
53	Buoyant $> 1$ m diameter pumice blocks floated to the ocean surface.
54	Clasts with enough isolated porosity and trapped gas floated in a raft while the rest sank.
55	
56	1. Introduction
57	
58	Submarine volcanic eruptions may be fundamentally different from those on land owing to the
59	high hydrostatic pressure provided by the ocean which inhibits degassing and hence magma
60	acceleration and fragmentation. Our understanding and record of such eruptions are limited by
61	the challenge in directly witnessing eruption processes and sampling and characterizing the
62	deposits from those eruptions. Indeed, overcoming this biased understanding of volcanic
63	eruptions was highlighted by the 2017 National Academies report (National Academies, 2017):
64	"What processes govern the occurrence and dynamics of submarine explosive eruptions"?
65	
66	Silicic magmas that erupt more than a few hundred meters below sea-level give rise to
67	eruption styles distinct from those on land owing to the contrasting properties of the ambient
68	fluid (water vs air) into which the magmas erupt (Cashman and Fiske, 1991). For example, clasts
69	that erupt at the seafloor are initially buoyant, but ingest water into pore space as they cool (e.g.,

Whitham and Sparks, 1986); hence fragmented magma can either rise to the surface to form
rafts, or feed submarine density currents if the clasts become waterlogged (Allen and McPhie,
2009).

73

74 One distinctive facies of both modern and ancient clastic deposits from submarine silicic 75 eruptions is voluminous deposits of giant (>1 m) pumice clasts (e.g., Kato, 1987; Kano et al., 76 1996; Kano, 2003; Allen and McPhie, 2009; Allen et al., 2010; Jutzeler et al., 2014). These clasts 77 often have one or more quenched margins with curviplanar joints perpendicular to the cooling 78 surface that suggest they quenched in water (e.g., Wilson and Walker, 1985; Allen et al., 2010; 79 Von Lichtan et al., 2016; Figure 1). Otherwise, submarine pumice vesicularities are similar to 80 those produced in subaerial Plinian eruptions (e.g., Barker et al., 2012) and hence it has been 81 proposed that fragmentation mechanisms are also similar for large (>  $1 \text{ km}^3$ ) submarine 82 equivalents (e.g., Allen and McPhie, 2009; Shea et al., 2013). There are, however, textural 83 differences: pumice clasts from deep submarine eruptions tend to have smaller bubble number 84 densities, lack very small vesicles (<10 µm), and display a narrower range of modal vesicle sizes 85 (Rotella et al., 2015). Clasts have also been proposed to form from buoyant bubbly magma as it 86 exits the vent by "viscous detachment or by the development of cooling joints" (Rotella et al., 87 2013), an eruption style that would not fit neatly into either the "effusive" or "explosive" 88 categories used to describe subaerial eruptions. Pumice clasts can also form by spallation from a 89 pumiceous carapace on effusive domes (e.g., Cas and Wright, 1987; Kano, 2003; Allen et al., 90 2010).

In July 2012, approximately 1.2 km<sup>3</sup> of rhyolite pumice clasts erupted at a water depth of 92 93 900 m from the submarine Havre volcano in the Kermadec volcanic arc (Carey et al., 2014; 94 Figure 1). The majority of the pumiceous material formed a raft of floating clasts that was widely 95 dispersed in the western Pacific Ocean (Jutzeler et al., 2014; Carey et al., 2018). A second clastic product of this eruption is a 0.1 km<sup>3</sup> deposit of giant pumice clasts on the seafloor around the 96 97 inferred vent. An outstanding question is whether these seafloor giant pumice clasts and raft 98 pumice originated from the same eruptive phase. Though not conclusive, the vesicularities, 99 composition, microtextures (e.g., bubble number densities, crystallinity, microlite mineralogy), 100 and macrotextures (e.g., banding), are similar as is their primary axis of dispersal (Carey et al., 101 2018). If the raft and seafloor pumice did originate from the same eruptive episode, their 102 different fate, i.e., whether they floated or sank, thus requires seafloor giant pumice to ingest 103 water more effectively than clasts that were transported into the raft.

104

Here we use a model for magma ascent, constrained by estimates of the eruption rate for the pumice raft and a variety of measurements on erupted materials, to show that buoyant magma reached the seafloor prior to fragmenting. We then investigate how pumice clasts from the raft and seafloor ingest water as they cool and find that seafloor pumice ingest water more efficiently by trapping very little gas. We thus infer that vesicular coherent magma extruded into the ocean. The magma quenched and fragmented non-explosively to form the pumice clasts that then either remained afloat because they retained enough gas or, if they waterlogged, settled to the seafloor.

113 **2. Methods** 

### 115 **2.1 Conduit model**

116

117 Magma ascent is simulated using a one-dimensional two-phase model for steady flow, modified 118 from Degruyter et al. (2012) and Kozono and Koyaguchi (2009). Pressure at the vent is 9 MPa 119 corresponding to a water depth of 900 m. The conduit length is 8.1 km with a pressure at its base 120 of 200 MPa. Crystallinity is 5% (Carey et al., 2018) and crystals do not grow or nucleate during 121 ascent. The effects of crystals and bubbles on viscosity are based on the models of Costa (2005) 122 and Llewellin and Manga (2005), respectively (supplement S1). Water content in the melt is 5.8 123 weight % based on 16 plagioclase-hosted melt inclusions from a seafloor giant pumice clast (supplement S2). Number density of bubbles is  $10^{14}$  m<sup>-3</sup> (Rotella et al., 2015), high enough that 124 125 we can assume equilibrium bubble growth (Gonnermann and Manga, 2005); we obtain similar 126 ascent rates for number densities 100 times lower and higher. The effects of temperature and 127 dissolved water on viscosity are computed using Giordano et al. (2008) and the measured 128 composition (supplement S3) and water content. Temperature is set to 850±20 °C based on cpx-129 opx Fe-Mg exchange (Putirka, 2008) in ten measured cpx and opx compositions. Magma can 130 fragment in the conduit if the strain-rate  $\dot{\gamma}$  exceeds a critical value (e.g., Papale, 1999) 131  $\dot{\gamma} > 10^{-2}G/\mu$ , (1)where  $G = 10^{10}$  Pa is the shear modulus (e.g., Simmons, 1998) and  $\mu$  is the melt viscosity. We 132

where  $G = 10^{-10}$  rais the shear modulus (e.g., Simmons, 1998) and  $\mu$  is the ment viscosity. We compute both the strain-rate at the conduit walls and the elongation strain-rate in the center of the conduit.

135

136 It is important to recognize that in addition to uncertainties in magma properties there are 137 also model assumptions that affect strain-rates, ascent velocity, and vesicularity at the vent. For example, the ascending magma is assumed to be isothermal and Newtonian, we neglect viscous heating and shear localization in the magma, and we do not permit non-equilibrium bubble growth. We also use a geometrically idealized conduit shape. In addition, we assume that at any given depth the bubble size is uniform and use this bubble size to compute a permeability. There are, however, bubbles much larger than the mean size which, owing to the nonlinearity of permeability-bubble size relationships, could lead to higher permeability and more outgassing.

145 **2.2 Floatation experiments** 

146

147 To determine the propensity for Havre pumice clasts to remain afloat after reaching the raft at the 148 ocean surface, we conducted 11 experiments in which we measured the amount of liquid water 149 and trapped gas within cm-sized clasts from the Havre raft (7 samples) and fragments of seafloor 150 giant pumice (4 samples). We heated dry raft clasts and giant pumice fragments to a range of 151 temperatures up to 700°C and placed them on the water surface for ten minutes. We then rapidly 152 encased the clasts in wax - to minimize further changes in the distribution of internal fluids -153 and imaged the clasts at 1.22 µm resolution using X-ray computed microtomography (XRT) with 154 30 keV monochromatic X-rays. To enhance the absorption contrast between the water and glass, 155 we used a 13 weight% potassium iodide solution. Additional imaging details are provided in 156 supplement S4. From the XRT images, we identified the volumetric content of glass, liquid 157 water, and trapped gas within the clasts using machine learning algorithms to segment these 158 three phases (Fauria et al., 2017).

160	To further quantify pumice floatation dynamics, we measured the floatation time of room
161	temperature raft and seafloor clasts. To measure floatation times, we placed dry and ambient
162	temperature clasts in water and noted the time at which they sank. Before the experiments, we
163	cleaned the clasts in an ultrasonicator for $\sim 10$ min and then dried them. Once the experiments
164	were initiated, we monitored the clasts with a camera and noted the time at which the clasts sank
165	to the nearest minute. If clasts continued to float after the first six months of the experiments, we
166	stopped monitoring with a camera and began checking on the clasts approximately daily and then
167	weekly once the experiments progressed past the first year.
168	
169	We measured clast weight before and after the experiments. For a subset of the clasts,
170	primarily the seafloor clasts, we measured clast volume using photogrammetry. Specifically, we
171	took 100-180 photographs per clast using a Canon DSLR camera with an extension tube. We
172	processed the images and constructed volume models (Poisson surface reconstructions) using
173	VisualSFM and MeshLab softwares. In cases where the clasts were too small to accurately
174	measure volume using photogrammetry, we estimate pumice volume using pumice mass
175	assuming a clast porosity of 83% (Carey et al., 2018).
176	
177	2.3 Isolated porosity
178	
179	Differences in isolated porosity between the raft and seafloor samples are unresolvable in
180	the XRT scans. We thus use helium pycnometry to quantify the connected and unconnected pore
181	space. Samples were cored, washed, dried, and weighed. The volume of the cylindrical cores
182	was calculated based on the mean of 10 measurements of the sample diameter and height. The

volume of the solid phase and isolated porosity was measured using a He-pycnometer at the
University of Oregon using methods described in Giachetti et al. (2010). The pycnometry
measurements and bulk volume were used to calculate the connected porosity. One seafloor
sample and one raft sample were crushed, weighed, and analyzed using He-pycnometry in order
to determine the solid density. The bulk vesicularity was calculated from the solid density, bulk
volume, and bulk density. The isolated vesicularity was calculated from the difference between
the bulk vesicularity and connected vesicularity.

190

191 **3. Results** 

192

193 Figure 2 shows how ascent velocity, mean bubble size, melt viscosity, and vesicularity 194 vary with depth in the conduit for conduit radii of 3, 21 and 33 m. The corresponding mass eruption rates are  $4.2 \times 10^3$ ,  $1.0 \times 10^7$  and  $6.2 \times 10^7$  kg/s respectively. This model reproduces the 195 observed vesicularity of about 80-90 % and modal vesicle size (Rotella et al., 2015; Carey et al., 196 197 2018). A conduit radius of 21 m leads to a mass eruption rate similar to the time-averaged value 198 inferred from the volume of the pumice raft and the estimated duration of the raft-forming stage 199 of the eruption,  $9 \times 10^6$  kg/s (Carey et al., 2018). For this eruption rate, Figure 2b shows that the 200 gas and melt remain coupled and there is negligible outgassing during ascent. The model does 201 not account for any further modification of vesicularity of clasts after they enter the ocean.

202

There are uncertainties in all model parameters including, critically, those that affect viscosity: water content and temperature. However, the main conclusions are not sensitive to reasonable ranges in these parameters. For example, if we reduce the water content to 5% and temperature to 820 °C, even for an eruption rate an order of magnitude greater than inferred,  $1 \times 10^8$  kg/s, the strain-rate is still a factor of 5 too low to cause melt to fragment based on equation (1).

209

210 Figure 3 shows that reheated (> 500°C) Havre raft pumice can retain enough gas to 211 remain buoyant. By comparison, fragments from the seafloor giant pumice are almost fully 212 saturated (< 0.05 volume fraction gas) after they are reheated above 500°C and placed on the 213 water surface. The results from these experiments demonstrate that hot Havre seafloor giant 214 pumice draw in considerably more water than raft pumice. In raft pumice, some of the gas is 215 trapped by the infiltrating water (red arrow), but there is also a significant amount of 216 unconnected porosity (isolated bubbles). This difference is further highlighted by the pycnometry 217 measurements. Figure 4 shows the connected and unconnected porosity analysis and reveals that 218 seafloor giant pumice has fully connected porosity whereas raft pumice always contains isolated 219 bubbles. These differences may be documenting samples from different parts of the conduit, or 220 samples that experienced different vesiculation histories in the water column. A thorough 221 analysis of textures from raft and seafloor samples may reveal not only why some clasts float, 222 but provide further insights into ascent processes in the conduit and water column.

223

Figure 5 shows clast volume versus floatation time. We identify clasts that were still floating at the time of manuscript submission with red outlines. We find that floatation time increases with clast size and that raft pumice float orders of magnitude longer than seafloor pumice. We compare pumice floatation times to a diffusion model for pumice floatation from Fauria et al. (2017). The model predicts that floatation time scales as

$$\tau = \frac{4R^2}{D_a\theta^2},\quad(2)$$

230	where $\tau$ is time, 2 <i>R</i> is clast diameter, $D_a = 1.9 \times 10^{-9} \text{ m}^2/\text{s}$ is air-water diffusivity (Fauria et al.,
231	2017), and $\theta$ is the fraction of pore space containing liquid water. The shaded region in Figure 5
232	shows predictions of equation (2) with $\theta$ between 0.1 and 0.5. Seafloor clasts match the diffusion
233	model prediction while raft pumice float much longer than predicted and, indeed, have yet to
234	sink. The presence of isolated bubbles (Figure 4) may explain why cold raft pumice float much
235	longer than theoretical models predict.
236	
237	
238	4. Discussion
239	
240	We now address in order three basic questions about the 2012 Havre eruption. Where and why
241	did the magma fragment? What processes form meter-sized clasts? Why do some pumice clasts
242	float (raft pumice) and others sink (seafloor giant pumice)?
243	
244	4.1 Fragmentation
245	
246	From the conduit model, strain rates never become large enough to cause brittle fragmentation
247	within the conduit of the Havre eruption. Instead, at 86% vesicularity, the erupting magma is less
248	dense than sea water and hence will continue to rise above the vent rather than creating a dome.
249	What processes then create the pumice? We do not favor buoyant detachment of blebs by
250	gravitational instabilities, one mechanism suggested for example by Rotella et al. (2013),

251 because the separation of blebs is slow compared to the inferred extrusion velocity for the Havre 252 eruption and we did not see fluidal-shaped clasts either near the vent or in samples from the raft. 253 For a bleb of length *l* and radius *r* buoyantly rising above the extruding magma, the velocity  $dl/dt \approx \frac{(\rho_w - \rho_c)gr^2}{\mu} \ln (l/r)$ , where  $\rho_c$  is clast density,  $\rho_w$  is water density, and g is gravity 254 255 (Olson and Singer, 1985). This is a Stokes flow scaling, appropriate because the magma 256 viscosity controls extrusion prior to fragmentation. Choosing l = 2r for equant bleb,  $\mu = 5 \times 10^6$ Pa s (Figure 2),  $\rho_w - \rho_c = 500$  kg m<sup>-3</sup> (Rotella et al., 2015; Carey et al., 2018), and *l*=5 m, we 257 258 obtain an ascent speed of 4 cm/s, much less than the velocity at the vent of 14 m/s (figure 2). The 259 melt is so viscous that ductile processes are too slow to produce clasts. 260 Instead, we suggest that the surface of extruded magma will quench in the ocean, producing a 261 network of cracks perpendicular to the magma surface. Highly vesicular magma is prone to 262 quench fragmentation and the temperature difference between magma and seawater is sufficient 263 to create cracks (van Otterloo et al., 2015), possibly aided by continued vesiculation. Crack 264 propagation speeds can be tens to hundreds of meters per second (van Oterloo et al., 2015) so 265 that a large volume of fragmented debris can be produced very quickly. Although a range of 266 fragment sizes will be produced, they will not be able to separate and rise unless they can also 267 float upwards fast enough from the extruding magma. Smaller fragments may weld together, or 268 may break off larger clasts or the side of the extruding spine of magma if the spine extends above 269 the vent.

270

271 *4.2 Separating pumice from extruding magma* 

The terminal rise speed U of clasts produced by quenching and surrounded by water, idealized here as spherical with radius R, is

275 
$$U = \sqrt{\frac{8(\rho_w - \rho_c)gR}{3\rho_w c_D}} \qquad (3)$$

Given the very high Reynolds number (~10<sup>7</sup>), the drag coefficient  $C_D$  is approximately 0.3 (e.g., 276 277 Batchelor, 1967). Equation (2) also neglects entrainment by the buoyant warm water heated by 278 the clasts, which would increase velocity. With a conduit radius of 21 m the vent velocity is 14 279 m/s (Figure 2), and clasts with R>4.5 m will rise faster than the extrusion speed, at least before 280 they ingest water. Exit velocity is inversely related to conduit radius owing to mass conservation. 281 If the vent widens by 40% at the seafloor, the minimum radius R for detachment decreases to 1.2 282 m. There are uncertainties in both the mass eruption rate that constrains the exit velocity and the 283 parameters that affect the minimum size of clasts computed from equation (3), but predicted 284 meter-sized clasts are similar to typical sizes of the giant pumice on the seafloor, averaging 1-1.6 285 m near the vent and increasing with dispersal distance (Carey et al., 2018).

286

#### 287 *4.3 Reaching the sea surface*

288

Clasts that detach from the extruded magma will rise through the ocean until they saturate with water. Once saturated, clasts will become negatively buoyant and sink to the seafloor. For metersized clasts, water ingestion is limited not by permeability but by the ability of water vapor in the clast to cool, condense and draw in liquid (appendix A). As cooling is slower than permeable flow, the rate of heat loss from the interior of the pumice will determine the time to saturation. To compute the evolution of clast density through water ingestion, and hence their ascent through the ocean, we model the cooling, condensation, and thus flow of liquid water into

296 spherically symmetric clasts using experimentally measured rates of heat loss, and compute the 297 rise speed of the clasts using equation (3) from the time-evolving mean clast density (assuming 298 fully connected porosity). We allow gas in the clasts to expand as the ambient pressure decreases (appendix B) which is significant because water vapor density is  $> 15 \text{ kg/m}^3$  at 900 m water 299 300 depth and  $\sim 1 \text{ kg/m}^3$  at the surface. Additional joints within clasts would enhance water ingestion 301 and cooling beyond what we model. We neglect any possible further vesiculation within clasts as 302 they rise through the ocean. Although clasts may remain hot as they ascend and can continue to 303 exsolve water, vesicles need not grow if the pore space is connected to permit gas leakage to the 304 ocean (e.g., Kueppers et al., 2012). Figure 6 shows the time required for clasts of different 305 vesicularities to reach the ocean surface before they become negatively buoyant in water. Meter-306 sized clasts, such as the seafloor giant pumice, are expected to reach the raft at the ocean surface 307 and will have ingested little water. The initial sizes of raft pumice are not known, but Figure 6 308 suggests that a minimum size of about one meter is required for clasts to reach the surface.

309

#### 310 *4.4 To sink or float?*

311

The long-term fate of floating pumice on the sea surface depends on their ability to ingest additional water as they float. The ascent model predicts that there is virtually no liquid in metersized and larger clasts as they reach the sea surface owing to the expansion of vapor in the clasts during ascent (appendix B). However, the seafloor deposit of giant pumice comprises clasts up to 9 m in diameter (Carey et al., 2018). Some of those may include pumices that are large enough to reach the sea surface, but are trapped underneath floating pumice and remain fully surrounded by water, in which case we would expect them to sink once the water vapor cools and condenses (Allen et al., 2008). Others must have reached the sea surface and subsequently saturated withwater.

321

322 Once pumice reaches the sea surface, we expect air to replace most of the water vapor in 323 the pore space because gas diffusion and exchange is rapid, and is further enhanced as clasts 324 crack or break. Air-filled pumice is known to float much longer (e.g., Whitham and Sparks, 325 1986; Manville et al., 1989; Dufek et al., 2007; Jutzeler et al., 2017) than the time it takes for 326 porous flow to allow water to infiltrate (Vella and Huppert, 2007). Instead, the ability of clasts to 327 float is controlled by the propensity of the infiltrating water to trap gas bubbles within the pore 328 space and/or the presence of isolated vesicles. If enough gas is trapped during infiltration of 329 water, the clasts will float until this gas diffuses through the water and out of the clast (Fauria et 330 al., 2017).

331

332 The difference in isolated and connected porosity can partially explain the propensity for 333 raft pumice to float, however, additional gas trapping is required for most clasts (Figure 4). Our 334 experiments confirm that fragments of seafloor giant pumice ingest more water and trap less gas 335 than raft pumice, and hence more rapidly become negatively buoyant. The presence of elongate 336 "tube" vesicles in some seafloor pumice has further implications for why some clasts sink 337 preferentially to others. The elongate structure, high connectivity and anisotropic permeability of 338 such vesicles would permit rapid clast saturation and subsequent sinking to the seafloor (Wright 339 et al., 2006). The diversity of these textures within pumice deserves more detailed microtextural 340 analysis.

341 We thus propose that what separates pumice into the raft is their ability to trap gas and 342 the presence of isolated vesicles; clasts that cannot retain enough gas sink. Those that trap gas 343 and/or have sufficient isolated vesicles float. Presumably the difference in gas trapping results 344 from differences in topology of the pore space such as the number of dead-end pores. We could 345 not, however, identify any key differences in our images. We note several caveats, however. 346 First, we are not able to do experiments on meter-sized raft or seafloor clasts owing to the lack of 347 intact samples and our inability to measure and image the infiltration at such large scales. We 348 thus assume that the smaller fragments we imaged are representative of the larger clasts from 349 their respective units. Second, we do experiments on quenched samples, whereas the vesicularity 350 and texture of the pumice may evolve during quenching and also after their initial fragmentation. 351 Larger clasts should take longer to ingest water, explaining why seafloor pumice clast size 352 increases with distance from the vent (Carey et al., 2018).

353

# 354 *4.5 The effusive eruption of Havre*

355

356 The raft-forming Havre eruption was not explosive in the same manner as subaerial pumice 357 clast-forming eruptions. This submarine style of pumice-generating eruption requires an eruption 358 depth that is not-too-deep and not-too-shallow (Figure 7). In deeper water, with the critical 359 depth depending on the water content of the melt, the magma will not be buoyant and will form a 360 lava flow or dome (Figure 7c). In shallower water, the melt viscosity will be higher owing to 361 greater gas exsolution and the magma may undergo brittle fragmentation in the conduit (Figure 362 7a). For the Havre mass eruption rate, composition, and water content, a vent depth of 2.8 km will lead to the erupting magma being denser than seawater (1030 kg/m<sup>3</sup>), and a vent shallower 363

364 than 290 m will allow the magma to fragment in the conduit (21 m radius) assuming that the 365 criterion given by equation (1) is accurate. It is worth noting that the Taupo eruption which also 366 produced giant pumice fragments, and was dominated by Plinian-phreatoplinian explosions and 367 magmatic fragmentation in the conduit, occurred in water depths that were never more than 200 368 m (Wilson and Walker, 1985; Houghton et al., 2003). Mass discharge rate also matters because 369 low ascent rates enable outgassing. For example, at Havre multiple lava domes with low-to-370 moderate vesicularity extruded in 2012 at the same water depth as the vent that produced the 371 giant pumice clasts. At Sumisu Dome C in the Sumisu Dome Complex, Izu Bonin Arc, Japan, 372 silicic pumiceous dome carapaces at 1100-1300 mbsl have high vesicularity, between 60 - 85%, 373 and did not produce a clastic deposit (Allen et al., 2010).

374

375 The 2012 eruption that produced the pumice raft partly conforms to the eruption style 376 proposed by Rotella et al. (2013) in which bubbly magma enters the ocean and clasts detach 377 from the extruding magma; we favor "cooling joints" and other mechanical stresses over 378 "viscous detachment" for Havre because the effusion velocity is so high and because we lack 379 evidence for any wholly or partly bleb-shaped clasts; ductile processes, however, may be 380 important for creating floating clasts from less viscous magmas (e.g., Kueppers et al., 2012). As 381 noted by others (e.g., Cas and Giordano, 2014; Allen and McPhie, 2009; White et al. 2015), 382 terminology such as explosive and effusive, developed for subaerial eruptions and their deposits, 383 may not translate well to the submarine realm where high hydrostatic pressure and the cooling 384 effects of liquid water can modulate fragmentation.

385

386	Given that submarine giant pumice deposits are common products of historical eruptions
387	and well documented in the rock record (Reynolds et al., 1980; Kano et al., 1996; Risso et al.,
388	2002; McPhie and Allen, 2003; Kano, 2003; Allen and McPhie, 2009; Allen et al., 2010; Jutzeler
389	et al., 2014; Von Lichtan et al., 2016), we infer that the 2012 Havre eruption may be an example
390	of a relatively common style of deep submarine volcanic eruption. Modern intra-oceanic arcs,
391	such as the Kermadec, Izu, Bonin, Mariana, and South Sandwich arcs contain many deep
392	submarine silicic volcanoes, and similar eruptions may be common.
393	
394	5. Conclusions
395	
396	The 2012 pumice raft-forming eruption was produced from a vent that extruded buoyant
397	vesicular rhyolite into the sea at speeds $> 10$ m/s. This lava fragmented by quenching in the
398	ocean to produce three subpopulations of clasts. Large clasts (> 1 m) rose to the sea surface
399	without ingesting enough water to sink. Those large clasts with sufficient isolated vesicles and/or
400	trapped gas remained afloat in the raft. Large clasts that did not retain enough gas, and those that
401	were trapped beneath the pumice raft, sank to create the seafloor giant pumice. Smaller clasts
402	would not have reached the surface, ingesting water quickly and settling close to the vent, or
403	were transported by currents if small enough.

404

405 The eruption style documented at Havre may be dominant for submarine silicic eruptions, as 406 most submarine vents are at depths greater than a few hundred meters. Giant pumice clasts are a 407 product, and thus an indicator, of large, deep effusive eruptions. This eruption style partitions 408 most of the mass into distal and global ocean basins, which has implications for how we interpret 409 past events and may ultimately lead to a re-evaluation of the volumes and magnitudes of410 submarine eruptions in the past.

411

412	Acknowledgements: MM, KF, CL and BH are supported by NSF 1447559. SM and BH are
413	supported by NSF 1357443. RJC was funded by the Australian Research Council
414	(DP110102196, DE150101190). AS is supported by NSF 1357216. MJ is supported by a
415	National Defense Science and Engineering Graduation Fellowship. XRT was enabled by the
416	Lawrence Berkeley National Lab Advanced Light source, beamline 8.3.2, and guidance from
417	Dula Parkinson. Additional support was provided by the Marsden fund and the 2017 Student
418	Mentoring and Research Teams (SMART) Program, Graduate Division, University of
419	California, Berkeley. Fumihiko Ikegami created Figure 1d. Brian Monteleone provided
420	assistance in SIMS analysis of melt inclusions at the Northeast National Ion Microprobe Facility.
421	Melissa Rotella provided the raft clasts using in the floatation experiments. Thomas Giachetti
422	provided assistance with He-pycnometry. We thank Tushar Mittal, Dan Fornari, Jocelyn McPhie,
423	Ray Cas and an anonymous reviewer for comments, and the rest of the MESH team and Roger
424	Revelle crew for making this science possible.
425	

426 Author contributions. MM and WD modeled magma ascent. KF and CL perfomed the
427 ingestion experiments and analysis. SM measured volatiles. CC measured composition. KF and
428 BH did the floatation experiments. MJ measured porosity. KF and MM developed the clast
429 ascent and ingestion model. All authors contributed to sample collection, interpretation and
430 writing.

## 433 Appendix

434

## 435 A. Why ingestion is not likely to be limited by permeability for large clasts

436

As the interior of vapor-filled pumice cools, vapor condenses and draws in liquid water. Whether
heat loss or permeability limits this ingestion of liquid depends on the ability of a clast to lose
heat compared to the ability of liquid to flow into the clast – the slowest process will govern
liquid ingestion.

441

The condensation of vapor and heat loss from the clast is similar to the classic Stefan problem except that advection of heat by liquid water drawn into the clast may dominate the heat transport. An energy balance at the vapor-liquid interface balances the conductive transport across that interface with the latent heat released

$$-\kappa \frac{dT}{dx} = \rho_s \phi L u \quad (A.1)$$

where *u* is the fluid velocity, *L* the latent heat,  $\rho_s$  is the density of steam,  $\phi$  is porosity, *T* is temperature,  $\kappa$  is the thermal conductivity of the liquid-saturated clast, and *x* is position. The temperature distribution within the liquid-saturated part of the clast that determines the left-hand side of equation (A.1) depends on *u*, and we use the solution for steady-state advective-diffusion problem from Bredehoeft and Papadopulos (1965)

$$\frac{T(x) - T_a}{T_s - T_a} = \frac{e^{\beta x/a} - 1}{e^{\beta} - 1} \quad (A.2)$$

452 where  $\beta = ua/D$  is a dimensionless Peclet number (ratio of advection to diffusion of heat),

453 where *D* is the thermal diffusivity of the liquid-saturated clast, *a* is the distance from the clast

454 surface to the steam-liquid interface, and  $T_a$  and  $T_s$  are the temperatures of the ambient water and

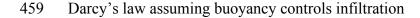
455 steam-liquid interface, respectively. The solution for the infiltration speed can be obtained by

456 solving equations (A.1) and (A.2)

$$u = \frac{D}{a} \ln \left[ 1 + \frac{\kappa (T_s - T_a)}{\rho_s \phi L D} \right] \quad (A.3)$$

457

458 If permeability limits the infiltration speed of water, a lower bound on the velocity is given by



$$u > \frac{k\rho_w g}{\mu_w \phi} \qquad (A.4)$$

460 where *k* is permeability, and  $\mu_w$  is the viscosity of water. We use > because we neglect the 461 additional (and likely much larger) pressure gradients from gas contraction and capillary forces 462 that would further increase *u*.

463

Whether heat loss controls infiltration (equation A.3) or permeable flow (equation A.4) depends
on which is larger – the slowest velocity is rate-limiting. Permeability is not limiting if

$$k > \frac{\mu_w \phi D}{a \rho_w g} \ln \left[ 1 + \frac{\kappa (T_s - T_a)}{\rho_s \phi L D} \right]$$
(A.5)

466

467 Using  $D = D_w \phi + D_r (1 - \phi) = 2.5 \times 10^{-7} \text{ m}^2/\text{s}$  for  $\phi = 0.8$ , where  $D_w$  and  $D_r$  are the

468 diffusivities of water and glass, respectively (Bagdassarov et al., 1994),  $\kappa = 2 \text{ Wm}^{-1}\text{K}^{-1}$ , and

469 conditions at the ocean surface ( $T_s - T_a = 100$  °C,  $\rho_s = 1$  kg/m<sup>3</sup>), we find that cooling is limiting

470 provided  $k > 1.5 \times 10^{-13}$  m<sup>2</sup> for a clast with a = 1 m. Permeability of pumice is generally larger

471	than this value, typically $> 10^{-12}$ m <sup>2</sup> for vesicularities of 70-80% (e.g., Rust and Cashman, 2004;
472	Mueller et al., 2005; Burgisser et al., 2017; Colombier et al., 2017; Gonnermann et al., 2018).
473	Note that the value of $k$ from equation (A.5) is an upper bound because we ignore additional
474	pressure gradients driving water into the clast in equation (A.4) and densities and temperature
475	difference at greater depths decrease the velocity predicted by equation (A.2). The model also
476	neglects any interfacial instabilities that might enhance infiltration or change effective
477	diffusivities (e.g., Randolph-Flagg et al., 2017).
478	
479	
480	B. Cooling, ingestion and ascent model
481	
482	We model the density evolution and rise of hot and initially water vapor-saturated clasts. Clast
483	density evolves due to internal gas decompression, contraction of vapor by cooling and
484	condensation, and from liquid water infiltration. We assume that the clast vesicularity does not
485	change due to volatile exsolution after clasts form. By coupling a model for clast density
486	evolution to a model for clast rise speed (equation 3), we can estimate the time it takes clasts of
487	varying sizes and vesicularities to reach the ocean surface from a depth of 900 m (Figure 6).
488	
489	Consider a clast that is entirely filled with water vapor such that $f = 1$ , where f is the fraction of
490	pore space filled with water vapor. The clast has vesicularity, $\phi$ , initial temperature, T, diameter,
491	D, and originates from a depth of 900 m. We assume an initial temperature of 850°C and
492	calculate the initial density $\rho_s$ , mass, $m_s$ , and specific enthalpy, $H$ , and total enthalpy, $H_T$ , of
493	internal the water vapor using a thermodynamic look-up table (IAPWS IF-97, XSteam;

Holmgren, 2006). We assume that the internal steam is fully coupled to the clast and cannot flow
out unless the volume of steam exceeds the internal volume of the clast pore space. We calculate
clast density as

497 
$$\rho_c = \rho_r (1 - \phi) + \rho_s \phi f + \rho_w \phi (1 - f)$$
 (B.1).

498

499 where the subscripts *r* and *w* stand for rock and liquid water. Clast density changes primarily as a 500 function of the volume of internal water vapor, which in turn is affected by cooling and 501 decompression. Clasts lose thermal energy through cooling according to

$$\frac{dH_T}{dt} = -qFS \qquad (B.2),$$

where q is an average rate of heat loss that was measured experimentally to be approximately 7.5 W cm<sup>-2</sup> for initially air-filled pumice in water (Fauria, 2017), *S* is clast surface area, and *F* is a factor that describes the partitioning of latent heat within the water vapor and sensible heat within the glass. The ratio of sensible to latent heat in the clasts is characterized by the Stefan number

507 
$$St = \frac{\Delta T c_p}{\phi L} \sim 1 \qquad (B.3),$$

508 where  $\Delta T$ , is the temperature difference between the initial clast temperature and ambient water, 509  $c_p$  is the heat capacity of the glass, and *L* is the latent heat of vaporization. We define

$$F = \frac{\phi L}{\Delta T c_p + \phi L} \qquad (B.4).$$

The factor *F* accounts for sensible heat loss from the glass. That is, not all heat is drawn out of the internal water vapor, rather a proportion of cooling affects the glass. For an 850°C clast, we estimate  $F \sim 0.5$ . We find that precise value for *F* does not affect the calculated clast rise speeds, but is important for determining the minimum clast size that can reach the surface.

515 We calculate clast rise speeds as a function of clast density and size using equation (3). Clast rise
516 distance *Z* through the water volume is

517

$$Z = \int U dt. \qquad (B.5)$$

518

We relate depth *h* to pressure according to  $P = \rho_w gh$ . At each new depth we calculate the density and volume,  $V_s$ , of the internal water vapor as a function of pressure and specific enthalpy using a thermodynamic lookup table (XSteam; Holmgren, 2006). Internal water vapor can expand as clasts rise through the water column, and contract due to cooling. The volume fraction of pore space filled with water vapor is

524 
$$f = \frac{V_s}{\phi V_c}.$$
 (B.6)

525

If the net effects of cooling, decompression, and gas expansion make the volume of internal water vapor exceed the volume of the pore space such that f > 1, we let all excess water vapor exit the pore space and set f = 1. We define the excess water vapor as  $E_x = f - 1$ . We write the change in water vapor mass and total enthalpy due to vapor escape from the clast as

$$\Delta m_i = -E_x V_c \phi \rho_{s,}$$
 (B.7)

 $\Delta H_T = -\Delta m_i H$ . (B.8)

- 530
- 531

532 In contrast, cooling can make contraction and condensation exceed decompression effects such 533 that f < 1. If this is the case, we allow water liquid water to enter to pore space vacated by steam 534 due to condensation (e.g., Fauria, 2017), but does not decrease the clast's enthalpy. Equation (B.1) demonstrates, however, how ingested water increases clast density and thereby affects rise
speed, decompression rates, and clast fate.

537

We solve equations (3) and (B.1-8) using a first order finite difference scheme. The model ends when a clast either reaches the ocean surface or becomes neutrally buoyant due to vapor condensation and water ingestion. Figure 4 shows how clast size affects rise time to the surface and the minimum clast sizes required to reach the surface from a depth of 900 m. Below these minimum clast sizes, cooling results in vapor condensation and buoyancy reversal before a clast can reach the surface (Figure 4).

544

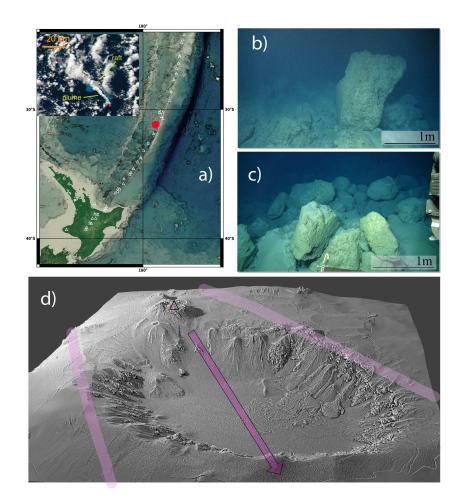
Many of the assumptions in equations (B.2-B.8) and approximations needed to develop this model could, in principle, be relaxed with a full 3D multiphase flow model that includes gas exsolution from the melt and mass, momentum and energy exchange with the surrounding water, and the presence of unconnected porosity (Figure 4). The model used here also neglects the buoyant ascent of warm water that would entrain clasts. A model that couples clast-scale processes and large scale dynamics may improve the accuracy of calculations of the fate of clasts and may reveal new and neglected processes.

552

553 If there is unconnected porosity, and all the connected porosity fills with liquid water, the 554 unconnected porosity is able to keep clasts floating if

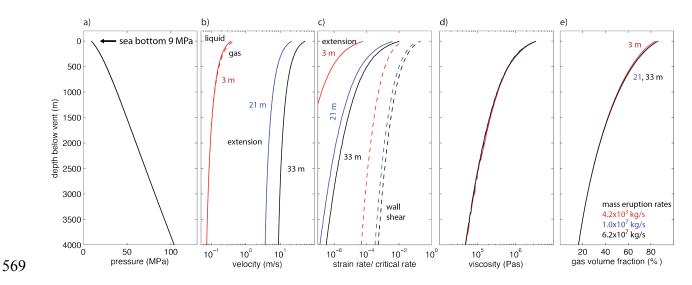
$$\phi_u = \frac{(\rho_r - \rho_w)}{(\rho_w - \rho_s)} (1 - \phi_t) \quad (B.9)$$

where the subscripts on density are as before and *u* and *t* indicate unconnected and total porosity,respectively.



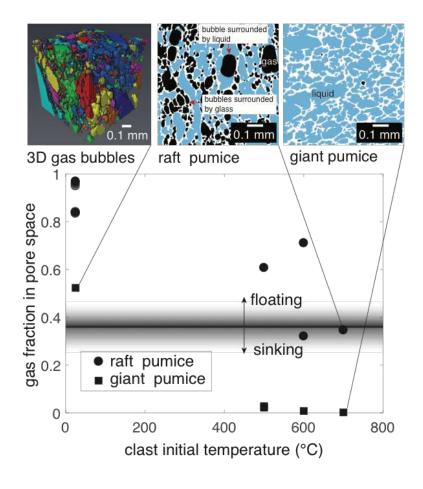
560

Figure 1: a) Location of the Havre volcano (red circle) in the Kermadec arc. Inset shows the raft and plume on 19 July, 01:26 UTC. Inset scale bar is 20 km long. Plume and raft show the transport direction to the northwest. Example seafloor giant pumice clasts showing curviplanar surfaces (b) and typical deposit (c). d) Shaded relief map showing the vent location (triangle) at a depth of 900 m; arrow shows the dispersal axis of seafloor giant pumice (the same as the transport direction in a), and the light purple lines bound the region containing those clasts. Caldera is 4.5 by 5 km in size. Viewing direction is looking south.



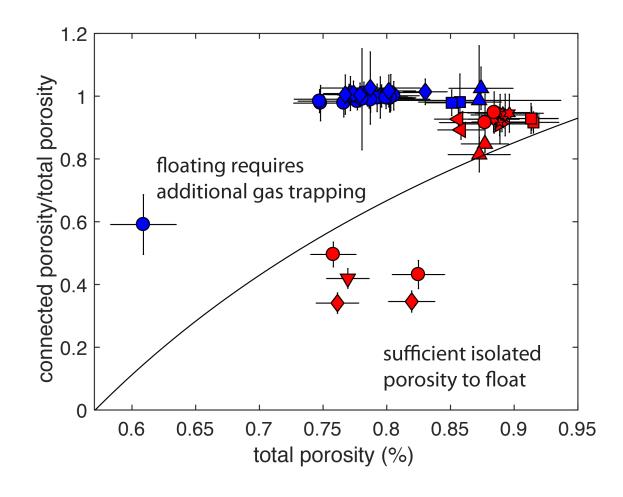
570 Figure 2: Magma ascent and gas escape, computed using the steady one-dimensional model of 571 Degruyter et al. (2012) with melt properties for the Havre 2012 rhyolite eruption, showing how 572 pressure (a), melt (solid curves) and gas (dashed curves) velocities (b), strain-rate relative to that 573 needed to cause brittle fragmentation (c), magma viscosity (d), and vesicularity (e) varies with 574 depth below the seafloor. Three conduit radii are assumed, 3, 21 and 33 m. Only the upper 4 km 575 of the conduit are shown. Additional parameters: the percolation threshold for gas flow through 576 the magma is zero, tortuosity factor is 3, bubble throat to radius ratio is 0.31, and the friction 577 coefficient for gas flow through the magma is 10 (supplement S1 for details).

579



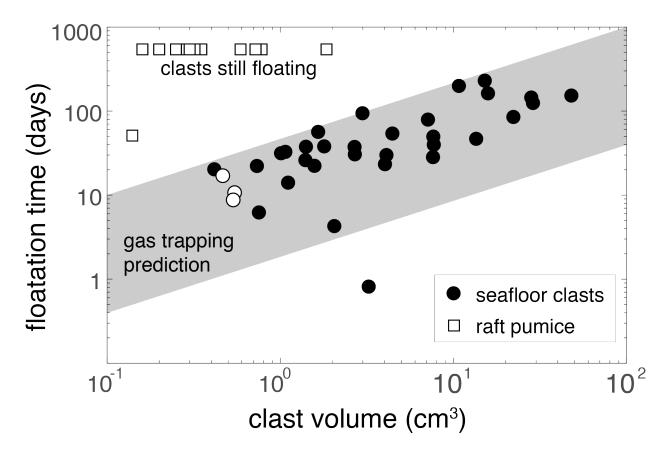
- 581
- 582

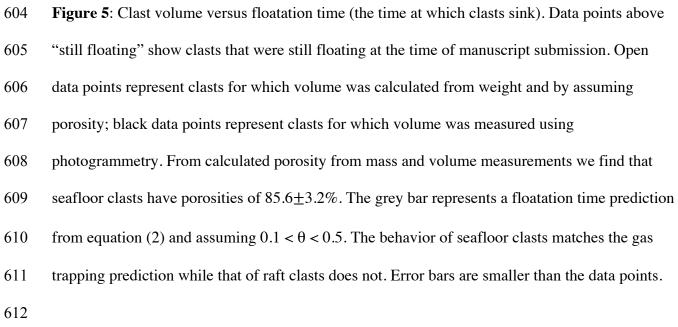
**Figure 3**: Initially hot pumice ingests more water than cold pumice, and giant pumice fragments (unknown locations within the larger clast) recovered from the seafloor ingest more water than pumice from the raft. A different pumice clast is used for each experiment and hence data point. The horizontal line shows the trapped gas fraction needed to keep a clast with a vesicularity of 80% buoyant. The two images on the upper right are 2D slices through their 3D images showing the distribution of glass (white), trapped gas (black), and liquid water (blue). Upper left shows the 3D shapes of trapped gas bubbles with a different color assigned to different gas bubbles.



590

592 Figure 4: Connected fraction of total porosity vs. total porosity for seafloor giant pumice 593 samples (red) and raft samples (blue). The measurements were conducted on multiple cores from 594 three seafloor giant pumice samples and nine raft samples. Distinct samples are shown with 595 different symbols. Excluding one seafloor measurement, which was collected from a 596 breadcrusted exterior, the seafloor giant pumice samples all have > 99% connected porosity. All 597 raft samples contain isolated vesicles. Shown with the curve is the amount of connected porosity 598 needed, as a function of total porosity to allow clasts to sink if the connected pore space fills 599 completely with water (equation B.9).





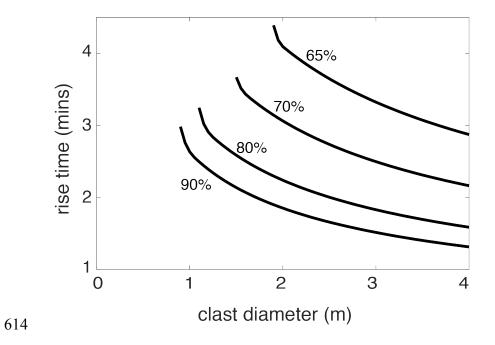
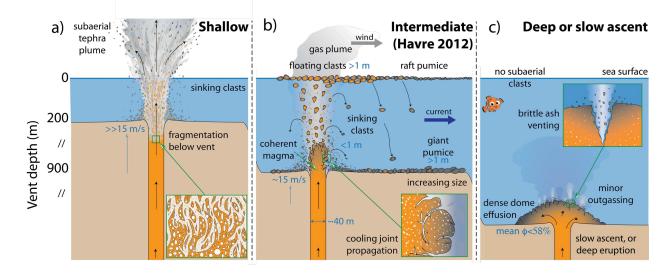


Figure 6: Time required for clasts to reach the ocean surface from a depth of 900 m as a function of their size and vesicularity (assumed constant during ascent). Clasts with diameters smaller than those for which the curves begin (to the left of the curves) will ingest enough water to become negatively buoyant before reaching the surface. Rise speed evolves according to equation (2) and clast density is computed from the water ingestion model (appendix B). 



623

624 Figure 7: Schematic illustration of the eruption of magma with Havre composition and water 625 content, but at different depths: a) shallow enough that fragmentation occurs in the conduit, b) 626 Havre vent depth, and c) deep or ascended slow enough that vesicularity is < 58%. In b), clast 627 size in the raft decreases with transport owing to abrasion. Inset in each panel illustrates the 628 manner in which clasts might form, either within the conduit (a), or quenching in water (b and c). 629 Panel b) illustrates the settling of smaller clasts close to the vent, the rise of large, hot clasts to 630 the sea surface, the trapping of hot pumice beneath the sea surface, and the settling of giant 631 pumice out of the raft due to water ingestion. The relative temperature gradient of melt to glass 632 in clasts given from orange to grey, respectively. White shapes are vesicles. Liquid water is blue. 633 Not to scale.

### 634 **References cited**

- Allen, R. L., Weihed, P., & Svenson, S. A. (1996). Setting of Zn-Cu-Au-Ag massive sulfide
- 636 deposits in the evolution and facies architecture of a 1.9 Ga marine volcanic arc, Skellefte
- 637 District, Sweden. *Economic Geology*, 91(6), 1022-1053.
- 638 Allen, S. R., Fiske, R. S., & Cashman, K. V. (2008). Quenching of steam-charged pumice:
- 639 Implications for submarine pyroclastic volcanism. *Earth and Planetary Science Letters*, 274(1),
  640 40-49.
- Allen, S. R., & McPhie, J. (2009). Products of neptunian eruptions. *Geology*, 37(7), 639-642.
- Allen, S. R., Fiske, R. S., & Tamura, Y. (2010). Effects of water depth on pumice formation in
- submarine domes at Sumisu, Izu-Bonin arc, western Pacific. *Geology*, 38(5), 391-394.
- Bagdassarov, N., & Dingwell, D. (1994). Thermal properties of vesicular rhyolite. *Journal of*
- 645 Volcanology and Geothermal Research, 60(2), 179-191.
- 646 Bredehoeft, J. D., & Papaopulos, I. S. (1965). Rates of vertical groundwater movement estimated
- 647 from the Earth's thermal profile. *Water Resources Research*, *1*(2), 325-328.
- 648 Barker, S. J., Rotella, M. D., Wilson, C. J., Wright, I. C., & Wysoczanski, R. J. (2012).
- 649 Contrasting pyroclast density spectra from subaerial and submarine silicic eruptions in the
- 650 Kermadec arc: implications for eruption processes and dredge sampling. *Bulletin of*
- 651 *volcanology*, 74(6), 1425-1443.
- 652 Batchelor, G. K. (1967). An Introduction to Fluid Mechanics, 615 pp. Cambridge University
- 653 Press, New York.
- Burgisser, A., Chevalier, L., Gardner, J. E., & Castro, J. M. (2017). The percolation threshold
- and permeability evolution of ascending magmas. *Earth and Planetary Science Letters*, 470, 37-
- 656 47.

- 657 Carey, R. J., Wysoczanski, R., Wunderman, R., & Jutzeler, M. (2014). Discovery of the largest
- historic silicic submarine eruption. *Eos, Transactions American Geophysical Union*, *95*(19), 157159.
- 660 Carey, R., Soule, S. A., Manga, M., White, J., McPhie, J., Wysoczanski, R., ... & Caratori-
- 661 Tontini, F. (2018). The largest deep-ocean silicic volcanic eruption of the past century. *Science*
- 662 *Advances*, 4(1), e1701121.
- 663 Cas, R. A. F., & Wright, J. V. (1987). Volcanic Successions, Modern and Ancient: A Geological
- Approach to Processes, Products and Successions, 528 pp.
- 665 Cas, R. A., & Giordano, G. (2014). Submarine volcanism: a review of the constraints, processes
- and products, and relevance to the Cabo de Gata volcanic succession. Italian Journal of
- 667 *Geosciences*, *133*(3), 362-377.
- 668 Cashman, K. V., & Fiske, R. S. (1991). Fallout of pyroclastic debris from submarine volcanic
- 669 eruptions. *Science(Washington)*, 253(5017), 275-280.
- 670 Colombier, M., Wadsworth, F. B., Gurioli, L., Scheu, B., Kueppers, U., Di Muro, A., &
- 671 Dingwell, D. B. (2017). The evolution of pore connectivity in volcanic rocks. *Earth and*
- 672 Planetary Science Letters, 462, 99-109.
- 673 Costa, A. (2005). Viscosity of high crystal content melts: dependence on solid
- 674 fraction. *Geophysical Research Letters*, *32*(22).
- 675 Degruyter, W., Bachmann, O., Burgisser, A., & Manga, M. (2012). The effects of outgassing on
- 676 the transition between effusive and explosive silicic eruptions. *Earth and Planetary Science*
- 677 *Letters*, *349*, 161-170.

- 678 Dufek, J., Manga, M., & Staedter, M. (2007). Littoral blasts: Pumice-water heat transfer and the
- 679 conditions for steam explosions when pyroclastic flows enter the ocean. Journal of Geophysical
- 680 Research: Solid Earth, 112(B11).
- 681 Fauria, K. (2017) PhD dissertation, University of California, Berkeley.
- Fauria, K. E., Manga, M., & Wei, Z. (2017). Trapped bubbles keep pumice afloat and gas
- diffusion makes pumice sink. *Earth and Planetary Science Letters*, 460, 50-59.
- 684 Giachetti, T., Druitt, T. H., Burgisser, A., Arbaret, L., & Galven, C. (2010). Bubble nucleation,
- growth and coalescence during the 1997 Vulcanian explosions of Soufrière Hills Volcano,
- 686 Montserrat. Journal of Volcanology and Geothermal Research, 193(3), 215-231.
- 687 Giordano, D., Russell, J. K., & Dingwell, D. B. (2008). Viscosity of magmatic liquids: a
- 688 model. *Earth and Planetary Science Letters*, 271(1), 123-134.
- 689 Gonnermann, H. M., & Manga, M. (2005). Nonequilibrium magma degassing: results from
- modeling of the ca. 1340 AD eruption of Mono Craters, California. *Earth and Planetary Science Letters*, 238(1), 1-16.
- 692 Gonnermann, H., Giachetti, T., Nguyen, C. T., Houghton, B. F., Crozier, J. A., & Carey, R. J
- 693 (2017). Permeability during magma expansion and compaction. Journal of Geophysical
- 694 Research: Solid Earth.
- Holmgren, M. (2006). X Steam for Matlab. www. x-eng. com, accessed November, 20, 2017.
- Houghton, B.F., Hobden, B.J., Cashman, K.V., Wilson, C.J.N. and Smith, R.T. (2003). Large-
- 697 Scale Interaction of Lake Water and Rhyolitic Magma During the 1.8 Ka Taupo Eruption, New
- 698 Zealand. Explosive subaqueous volcanism, pp. 97-109.

- Jutzeler, M., Marsh, R., Carey, R. J., White, J. D., Talling, P. J., & Karlstrom, L. (2014). On the
- fate of pumice rafts formed during the 2012 Havre submarine eruption. *Nature*
- 701 communications, 5.
- Jutzeler, M., Manga, M., White, J. D. L., Talling, P. J., Proussevitch, A. A., Watt, S. F. L.,
- 703 Cassidy, R.N., Le Friant, A., & Ishizuka, O. (2017). Submarine deposits from pumiceous
- 704 pyroclastic density currents traveling over water: An outstanding example from offshore
- 705 Montserrat (IODP 340). *Geological Society of America Bulletin*, *129*(3-4), 392-414.
- Kano, K. (2003). Subaqueous pumice eruptions and their products: A review. *Explosive*
- 707 subaqueous volcanism, 213-229.
- 708 Kano, K., Yamamoto, T., & Ono, K. (1996). Subaqueous eruption and emplacement of the
- 709 Shinjima Pumice, Shinjima (Moeshima) Island, Kagoshima Bay, SW Japan. Journal of
- 710 Volcanology and Geothermal Research, 71(2-4), 187-206.
- 711 Kato, Y. (1987). Woody pumice generated with submarine eruption. *Journal of the Geological*
- 712 Society of Japan, 93, 11-20 (1987).
- 713 Kozono, T., & Koyaguchi, T. (2009). Effects of relative motion between gas and liquid on 1-
- 714 dimensional steady flow in silicic volcanic conduits: 2. Origin of diversity of eruption
- styles. *Journal of Volcanology and Geothermal Research*, *180*(1), 37-49.
- 716 Kueppers, U., Nichols, A.R.L., Zanon, V., Potuzak, M., Pacheco, J.M.R., 2012. Lava balloons -
- 717 peculiar products of basaltic submarine eruptions. Bull. Volcanol. 74, 1379–1393.
- 718 Llewellin, E. W., & Manga, M. (2005). Bubble suspension rheology and implications for conduit
- flow. Journal of Volcanology and Geothermal Research, 143(1), 205-217.

- 720 Manville, V., White, J. D. L., Houghton, B. F., & Wilson, C. J. N. (1998). The saturation
- behaviour of pumice and some sedimentological implications. *Sedimentary Geology*, *119*(1), 516.
- 723 McPhie, J., & Allen, R. L. (2003). Submarine, Silicic, Syn-Eruptive Pyroclastic Units in the
- 724 Mount Read Volcanics, Western Tasmania: Influence of Vent Setting and Proximity on
- 725 Lithofacies Characteristics. *Explosive Subaqueous Volcanism*, 245-258.
- 726 Mitchell, S. J., McIntosh, I. M., Houghton, B. F., Carey, R. J., & Shea, T., (in review). Dynamics
- of a powerful deep submarine eruption recorded in H2O contents and speciation in rhyolitic
- glass: The 2012 Havre eruption, *Earth and Planetary Science Letters*
- 729 Mueller, S., Melnik, O., Spieler, O., Scheu, B., & Dingwell, D. B. (2005). Permeability and
- 730 degassing of dome lavas undergoing rapid decompression: an experimental
- 731 determination. *Bulletin of Volcanology*, 67(6), 526-538.
- 732 National Academies of Sciences, Engineering and Medicine (2017). Volcanic eruptions and their
- repose, unrest, precursors, and time. Washington, DC: The National Academies Press.
- 734 https://doi.org/10.17226/24650.
- 735 Olson, P., & Singer, H. (1985). Creeping plumes. Journal of Fluid Mechanics, 158, 511-531.
- 736 Papale, P. (1999). Strain-induced magma fragmentation in explosive
- rature, *397*(6718), 425-428.
- 738 Putirka, K. D. (2008). Thermometers and barometers for volcanic systems. *Reviews in*
- 739 *Mineralogy and Geochemistry*, 69(1), 61-120.
- 740 Randolph-Flagg, N., Breen, S., Hernandez, A., Manga, M., & Self, S. (2017). Evenly spaced
- columns in the Bishop Tuff (California, USA) as relicts of hydrothermal
- 742 cooling. *Geology*, 45(11), 1015-1018.

- 743 Reynolds, M. A., Best, J. G., & Johnson, R. W. (1980). 1953-57 Eruption of Tuluman Volcano:
- 744 Rhyolitic Volcanic Activity in the Northern Bismarck Sea (Vol. 7). Geological Survey of Papua
- 745 New Guinea.
- 746 Risso, C., Scasso, R. A., & Aparicio, A. (2002). Presence of large pumice blocks on Tierra del
- Fuego and South Shetland Islands shorelines, from 1962 South Sandwich Islands
- 748 eruption. *Marine Geology*, *186*(3), 413-422.
- 749 Rotella, M. D., Wilson, C. J., Barker, S. J., & Wright, I. C. (2013). Highly vesicular pumice
- generated by buoyant detachment of magma in subaqueous volcanism. *Nature Geoscience*, 6(2),
- 751 129.
- 752 Rotella, M. D., Wilson, C. J., Barker, S. J., Schipper, C. I., Wright, I. C., & Wysoczanski, R. J.
- 753 (2015). Dynamics of deep submarine silicic explosive eruptions in the Kermadec arc, as reflected
- in pumice vesicularity textures. Journal of Volcanology and Geothermal Research, 301, 314-
- 755 332.
- Rust, A. C., & Cashman, K. V. (2004). Permeability of vesicular silicic magma: inertial and
- hysteresis effects. *Earth and Planetary Science Letters*, 228(1), 93-107.
- Shea, T., Hammer, J., & First, E. (2013). Magma balloons or bombs? *Nature Geoscience*, 6(10),
  802-803.
- 760 Simmons, J. H. (1998). What is so exciting about non-linear viscous flow in glass, molecular
- 761 dynamics simulations of brittle fracture and semiconductor-glass quantum composites. Journal
- 762 of non-crystalline solids, 239(1), 1-15.
- Vella, D., & Huppert, H. E. (2007). The waterlogging of floating objects. *Journal of Fluid Mechanics*, 585, 245-254.

- van Otterloo, J., Cas, R. A., & Scutter, C. R. (2015). The fracture behaviour of volcanic glass and
- relevance to quench fragmentation during formation of hyaloclastite and
- 767 phreatomagmatism. Earth-Science Reviews, 151, 79-116.
- von Lichtan, I. J., White, J. D. L., Manville, V., & Ohneiser, C. (2016). Giant rafted pumice
- 769 blocks from the most recent eruption of Taupo volcano, New Zealand: Insights from
- palaeomagnetic and textural data. *Journal of Volcanology and Geothermal Research*, 318, 73-88.
- 771 White, J.D., Schipper, C.I. and Kano, K. (2015). Submarine explosive eruptions. In The
- 772 Encyclopedia of Volcanoes (Second Edition) (pp. 553-569).
- 773 Whitham, A. G., & Sparks, R. S. J. (1986). Pumice. Bulletin of Volcanology, 48(4), 209-223.
- Wilson, C. J. N., & Walker, G. P. (1985). The Taupo eruption, New Zealand I. General
- aspects. Philosophical Transactions of the Royal Society of London A: Mathematical, Physical
- 776 and Engineering Sciences, 314(1529), 199-228.
- 777 Wright, H., Roberts, J.J., Cashman, K.V., 2006. Permeability of anisotropic tube pumice: model
- calculations and measurements. Geophys. Res. Lett. 33 (17).
- 779

## 780 S1 Conduit model parameters

781

Magma ascent is modeled assuming steady isothermal two-phase flow in a cylindrical conduit
with constant radius. The flow is one-dimensional with all properties varying only with depth.
The equations solved are identical to those in Degruyter et al. (2012) with fragmentation
criterion given by (1) and a few modifications. We fit a model for melt viscosity with the same
functional form as that in Hess and Dingwell (1996) with viscosity computed from Giordano et
al. (2008) and measured composition (S3),

$$\log \mu = -3.62517 + 0.248398 \ln(100c) + \frac{9601 - 2368 \ln(100c)}{T - (195.7 + 96.4931 \ln(100c))}$$

788 where *c* is the water concentration in mass fraction and *T* is temperature.

789 The magma viscosity  $\mu_m$  is given by

$$\mu_m = \mu(c,T)\theta(\chi)\nu(\phi)$$

where  $\theta(\chi)$  accounts for the effects of crystals (5% assumed) on magma viscosity (Costa, 2005), and

$$v(\phi) = (1-\phi)^{5/3}$$

accounts for the effects of bubbles (Llewellin and Manga, 2005).

793

Other parameters used in the model include a gas viscosity of  $10^{-5}$  Pa s, a conduit length of 8100

795 m, magma temperature of 850 °C, melt density of 2400 kg m<sup>-3</sup>, initial water content of 5.8 weight

796 %, initial pressure of 200 MPa, vent pressure of 9 MPa, bubble number density of  $10^{14}$  m<sup>-3</sup>,

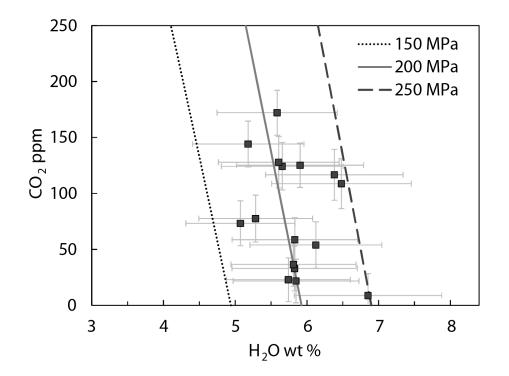
- tortuosity factor *m* of 3, friction factor  $f_0$  of 10, a throat/bubble size ratio  $f_{tb}$  of 0.3125, and a
- 798 percolation threshold of 0 (continuous percolation).

- 800 References for S1
- 801
- 802 Costa, A. (2005). Viscosity of high crystal content melts: dependence on solid fraction. Geophysical Research 803
- Letters, 32(22).
- 804 Degruyter, W., Bachmann, O., Burgisser, A., & Manga, M. (2012). The effects of outgassing on the transition
- 805 between effusive and explosive silicic eruptions. Earth and Planetary Science Letters, 349, 161-170.
- 806 Giordano, D., Russell, J. K., & Dingwell, D. B. (2008). Viscosity of magmatic liquids: a model. Earth and
- 807 Planetary Science Letters, 271(1), 123-134.
- 808 Hess, K. U., & Dingwell, D. D. (1996). Viscosities of hydrous leucogranitic melts: A non-Arrhenian
- 809 model. American Mineralogist, 81(9-10), 1297-1300.
- 810 Llewellin, E. W., & Manga, M. (2005). Bubble suspension rheology and implications for conduit flow. Journal of
- 811 Volcanology and Geothermal Research, 143(1), 205-217.

815	Initial dissolved volatile contents c were measured using the CAMECA IMS 1280 secondary ion
816	mass spectrometer at Woods Hole Oceanographic Institution, Massachusetts. H <sub>2</sub> O, CO <sub>2</sub> and F
817	contents were obtained from 16 plagioclase-hosted melt inclusions from a giant pumice block
818	retrieved from the seafloor (Carey et al., in press). Melt inclusions analyzed ed had no visible
819	fractures or pathways to the phenocryst edge and no vapor bubbles present.
820	
821	Raw ${}^{16}O^{1}H/{}^{30}Si$ ratios from the SIMS were calibrated to $H_2O$ wt % using calibration curves
822	determined from a series of rhyolite standards and synthetic forsterite with known FTIR $H_2O$ wt
823	%. Likewise, CO <sub>2</sub> and F were determined using the raw ${}^{12}C/{}^{30}Si$ and ${}^{35}F/{}^{30}Si$ ratios from the
824	samples and known CO <sub>2</sub> and F calibration curves from the standards. Measurements are
825	summarized in Table S2.1.
826	
827	H <sub>2</sub> O and F contents were used in the initial melt viscosity calculation (supplement S1); F
828	contents <0.1 wt % (1000 ppm) had a negligible effect on viscosity. Figure S2.1 shows that $H_2O$
829	and CO <sub>2</sub> contents were also used to determine the initial model pressure of 200 MPa using the
830	VolatileCalc solubility model (Newman and Lowenstern, 2002). H <sub>2</sub> O-CO <sub>2</sub> isobars were
831	determined for a rhyolitic melt at 850°C where all melt inclusions correspond to an average
832	storage pressure of 200 MPa. The very low CO <sub>2</sub> contents (<150 ppm) justifies the use of only
833	$H_2O$ as the volatile phase within the conduit ascent model (S1).

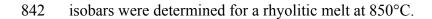
836 Table S2.1 Measured volatile contents in melt inclusions of seafloor pumice clasts837

SIMS data	H <sub>2</sub> O (wt %)	CO <sub>2</sub> (ppm)	F (ppm)
Havre melt	5.74	22.8	963
inclusions	6.12	53.9	992
	5.66	124.3	955
	5.07	73.3	888
	6.85	8.8	970
	5.29	77.5	838
	5.83	58.6	996
	5.90	125.2	985
	5.83	33.0	966
	6.38	116.7	1040
	6.48	108.7	1054
	5.58	172.1	935
	5.61	127.9	931
	5.85	21.8	978
	5.81	36.5	901
	5.18	144.1	1022
Average	5.82	81.6	963



840

841 Figure S2.1 Measured CO<sub>2</sub> and H<sub>2</sub>O in plagioclase-hosted melt inclusions with H<sub>2</sub>O-CO<sub>2</sub>



844 References for S2

845

- 846 Newman, S., & Lowenstern, J. B. (2002). VolatileCalc: a silicate melt-H<sub>2</sub>O-CO<sub>2</sub> solution model written in Visual
- 847 Basic for Excel. Computers & Geosciences, 28(5), 597-604.

010 031	/ L/	• • •
849 S3 M	<b>lelt comp</b>	osition

- XRF data given in Table S3.1 are the average for 5 giant pumiceous blocks sampled from the
- seafloor. Values match very well with those from Carey et al. (in press) and Rotella et al.,
- (2015). Fe<sub>2</sub>O<sub>3</sub> is corrected to FeO<sub>t</sub> for use in the viscosity model (supplement S1).

854

We assume the initial melt composition is the same as the whole rock plus dissolved water.

856

857 **Table S3.1** Whole rock composition.

SiO <sub>2</sub>	TiO <sub>2</sub>	Al <sub>2</sub> O <sub>3</sub>	FeO <sub>t</sub>	MnO	MgO	CaO	Na <sub>2</sub> O	K <sub>2</sub> O	P <sub>2</sub> O <sub>5</sub>	Total	LOI
72.437	0.479	14.145	3.017	0.122	0.727	2.608	5.117	1.590	0.083	100.325	1.131

858

## 859 S4 X-ray computed microtomography

860

861 X-ray microtomography was performed on beamline 8.3.2 at the Advanced Light Source,

862 Lawrence Berkeley National Lab. We used 30 kev monochromatic x-rays, a 5X lens to obtain a

voxel size of 1.22 microns, and used 1024 images and the TomoPy gridrec algorithm (Gursoy et

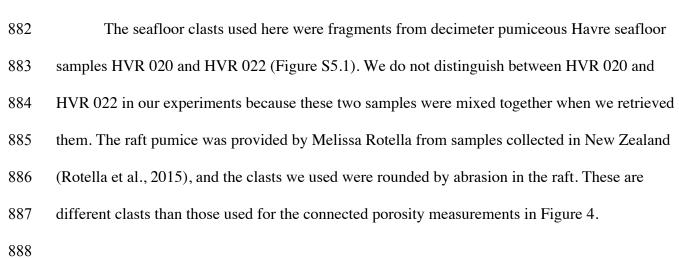
al., 2014) to create the 3D images.

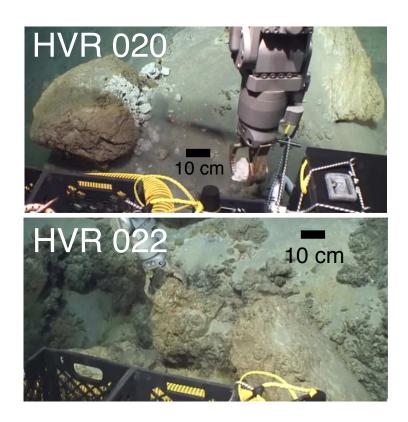
- 866 To segment the 3D images into water, gas and glass, we used the Fiji trainable Weka
- 867 segmentation algorithm (Hall et al., 2009) by manually outlining gas, liquid and glass and
- 868 retraining the classifiers until the segmentation seemed accurate. The volume fraction of each
- 869 phase was computed from the binary segmented images in Fiji. Aviso was used to make the
- 870 images in Figure 4 and to identify distinct bubbles in the 3D rendering.

- 871
- 872 References cited in S4
- 873
- 874 Gürsoy, D., De Carlo, F., Xiao, X., & Jacobsen, C. (2014). TomoPy: a framework for the analysis of synchrotron
- tomographic data. *Journal of synchrotron radiation*, *21*(5), 1188-1193.
- 876 Hall, M., Frank, E., Holmes, G., Pfahringer, B., Reutemann, P., & Witten, I. H. (2009). The WEKA data mining
- 877 software: an update. *ACM SIGKDD explorations newsletter*, *11*(1), 10-18.
- 878
- 879

## 880 Supplement S5: Pumice floatation experiments

881





- 890 Figure S5.1: Havre seafloor clasts used in the pumice floatation experiments. HVR 020 and
- 891 HVR 022 are both decimeter pumiceous clasts. The images show the clasts at the time of sample
- 892 collection (Carey et al., in press).

**Table S5.1** Experimental results and measurements of pumice floatation time. \* refers to values

that were calculated assuming a clast porosity of 83% and "nd" means not directly measured.

						floatation time
	pumice name	type	weight (g)	volume (cm^3)	porosity	(days)
•	MDR_01	raft	0.058	*0.14	nd	51.03
	MDR_02	raft	0.141	*0.35	nd	> 532
	MDR_03	raft	0.132	*0.32	nd	> 532
	MDR_04	raft	0.064	*0.16	nd	> 532
	MDR_05	raft	0.116	*0.28	nd	> 532
	MDR_06	raft	0.082	*0.20	nd	> 532
	S1_07	raft	0.755	*1.85	nd	> 532
	S1_08	raft	0.319	*0.78	nd	> 532
	S1_09	raft	0.241	*0.59	nd	> 532
	S1_10	raft	0.292	*0.72	nd	> 532
	S1_11	raft	0.121	*0.30	nd	> 532
	S1_12	raft	0.294	*0.72	nd	> 532
	S1_13	raft	0.1	*0.25	nd	> 532
	S1_14	raft	0.034	*0.08	nd	> 532
	HVR 001	seafloor	1.646	4.14	0.83	29.4
	HVR 002	seafloor	1.048	2.71	0.84	36.7
	HVR 003	seafloor	0.71	2.07	0.86	4.2
	HVR 004	seafloor	0.238	1.02	0.90	30.9
	HVR 005	seafloor	0.646	1.67	0.84	55.5
	HVR 006	seafloor	0.647	1.59	0.83	21.9
	HVR 007	seafloor	0.177	0.42	0.82	19.9
	HVR 008	seafloor	0.349	1.08	0.87	32.1
	HVR 009	seafloor	0.567	1.41	0.83	25.6
	HVR 010	seafloor	0.404	0.76	0.78	6.1

HVR 011	seafloor	0.446	1.42	0.87	36.9
HVR 012	seafloor	0.249	0.74	0.86	21.8
HVR 013	seafloor	0.423	1.12	0.84	13.8
HVR 015	seafloor	0.905	3.01	0.88	92.5
HVR 016	seafloor	0.228	0.54	0.83	8.6
HVR 017	seafloor	0.192	*0.47	nd	16.7
HVR 018	seafloor	1.747	3.27	0.78	0.8
HVR 018	seafloor	1.747	3.27	0.78	0.8
HVR 019	seafloor	0.539	1.81	0.88	37.3
HVR 020	seafloor	0.925	2.72	0.86	30
HVR 021	seafloor	5.465	15.97	0.86	159.5
HVR 022	seafloor	9.931	22.38	0.82	83.5
HVR 023	seafloor	14.601	29.04	0.79	122.5
HVR 024	seafloor	22.521	48.37	0.81	150.1
HVR 025	seafloor	0.224	*0.55	nd	10.5
HVR 026	seafloor	11.432	28.39	0.83	142.1
HVR 028	seafloor	6.632	13.65	0.80	45.9
HVR 030	seafloor	0.222	*0.54	nd	8.6
HVR 031	seafloor	5.481	15.30	0.85	225.6
HVR 032	seafloor	4.121	7.72	0.78	48.7
HVR 033	seafloor	1.461	4.06	0.85	22.9
HVR 034	seafloor	2.252	4.48	0.79	53
HVR 035	seafloor	2.817	7.19	0.84	77.7
HVR 036	seafloor	3.648	10.85	0.86	195.5
HVR 037	seafloor	3.69	7.77	0.80	39.1
HVR 038	seafloor	2.803	7.69	0.85	27.8